JES Focus Issue on Progress in Molten Salts and Ionic Liquids

Physical and Electrochemical Investigations into Blended Electrolytes Containing a Glyme Solvent and Two Bis{(trifluoromethyl)sulfonyl}imide-Based Ionic Liquids

Alex R. Neale,[a,z] Peter Goodrich,[a] Terri-Louise Hughes,[a,b] Christopher Hardacre,[a,b] Sarah C. Ball,[c,*] and Johan Jacquemin[a,d,z]

[a]*School of Chemistry and Chemical Engineering, Queen's University Belfast, Belfast, Northern Ireland BT9 5AG, United Kingdom*
[b]*School of Chemical Engineering and Analytical Science, University of Manchester, Manchester M13 9PL, United Kingdom*
[c]*Johnson Matthey Technology Centre, Sonning Common, Reading RG4 9NH, United Kingdom*
[d]*Université François Rabelais, Laboratoire PCM2E, Parc de Grandmont 37200 Tours, France*

In this paper, we report on thermophysical and electrochemical investigations of a series of molecular solvent/ionic liquid (IL) binary mixture electrolytes. Tetraethylene glycol dimethyl ether (TEGDME) is utilized as the molecular solvent component in separate mixtures with two bis{(trifluoromethyl)sulfonyl}imide anion based ILs paired with similarly sized cyclic and acyclic alkylammonium cations; 1-butyl-1-methylpyrrolidinium bis{(trifluoromethyl)sulfonyl}imide, [$Pyrr_{14}$][TFSI], or *N*-butyl-*N*,*N*-dimethyl-*N*-ethylammonium bis{(trifluoromethyl)sulfonyl}imide, [N_{1124}][TFSI]. The blending of ILs with select molecular solvents is an important strategy for the improvement of the typically sluggish transport capabilities of these interesting electrolytic solvents. Bulk volumetric and transport properties are reported as a function of temperature and binary mixture formulation; demonstrating the capacity for enhancing desired properties of the IL. Micro-disk electrode voltammetry and chronoamperometry in O_2-saturated binary mixture electrolytes was used to assess the effect of formulation on the solubility and diffusivity of the dissolved gas. In addition, further investigations of the behavior of the O_2 redox couple at a GC macro-disk electrode are discussed.
 [DOI: 10.1149/2.0141708jes]

Manuscript submitted February 14, 2017; revised manuscript received April 13, 2017. Published May 6, 2017. This was Paper 84 presented at San Diego, California, Meeting of the Society, May 29- June 2, 2016. *This paper is part of the JES Focus Issue on Progress in Molten Salts and Ionic Liquids.*

The exploration of ionic liquids (ILs) as alternatives to conventional molecular solvents in electrolyte formulations is continually growing for a variety of electrochemical applications. These low melting organic salts can be tailored to exhibit a variety of properties, including hydrophobicity and thermal, chemical, and electrochemical stability, which make them attractive candidate electrolyte solvents. Composed solely of ionic components, ILs consequently possess intrinsic electrolytic conductivity and are additionally non-volatile. These properties have encouraged the use of ILs as (complete or partial) substitutions of the volatile components of commercial Li-ion batteries, electrochemical double layer capacitors (EDLCs), and other prospective battery technologies (e.g. Na-ion, Mg-ion and metal-air batteries) for the development of potentially safer devices.[1–15] Furthermore, the high (electro)chemical stabilities and non-volatilities exhibited by many IL structures provides interesting electrolyte media for electrochemical gas sensors (e.g. for O_2,[16–19] CO_2,[20,21] NO_2[22]) where traditional solvents are prone to evaporation leading to device failure, and also for electromechanical actuator,[23–25] and electrodeposition applications.[26–28]

Nevertheless, while the properties of ILs are dependent on the virtually unlimited combinations of different cation and anion structures, the attractive features are generally coupled with sluggish transport properties relative to conventional electrolytes based on either aqueous or organic solvents. In turn, electrochemical devices constructed with neat IL electrolytes are likely to suffer transport limitations on useable current rates for the given application, for example restricting power capabilities of storage devices and response times for electrochemical sensors.

In the scope of addressing the shortcomings of IL materials for electrolyte applications, structural modifications of the constituent ions may be utilized to fine-tune the properties of the resulting IL. However, present state-of-the-art developments of novel IL materials have yet to yield sufficient promotions in transport properties without the sacrifice of other vital features. For example, we recently reported the characterization of newly synthesized ILs based around ethereal/alkyl-functionalized sulfonium cations paired with the bis{(trifluoromethyl)sulfonyl}imide, $[TFSI]^-$, anion.[29] Such anion/cation combinations yielded ILs with comparatively low viscosities/good conductivities but lower thermal and electrochemical stabilities when compared with ILs based on analogous alkyl-functionalized ammonium or phosphonium aprotic cations.[30,31] Alternatively, ILs may be blended with appropriate, lower viscosity organic molecular solvents with the goal of exploiting the positive aspects of the respective components. Therein, these aspects primarily relate to improved transport properties of the molecular solvent component and the potential to improve safety and stability issues with the IL. The mutual solubility between many ILs and common non-aqueous electrochemical solvents enable the consideration of a wide range of formulations in a given mixture with the prospect of balancing the desired properties. As such, investigating the application of IL/molecular solvent blends as electrolytes for Li-ion batteries,[1–4] Na-ion batteries,[13] Li-O_2 chemistry,[32–34] and EDLCs,[7–10] has continually revealed material benefits relating to electrolyte stability and device safety.

Herein, this work details the thermophysical characterization and electrochemical investigations of a series of IL binary mixtures with tetraethylene glycol dimethyl ether (TEGDME) for potential electrolyte applications. As part of the dipolar aprotic family of glyme solvents, TEGDME exhibits intermediate associative strength and good (electro)chemical stabilities. However, the longer chain structure affords this glyme solvent with lower vapor pressure and volatility than the shorter chain glyme analogues. Physical characterization of (*X*)[$Pyrr_{14}$][TFSI] – (1-*X*)TEGDME binary mixtures, where $[Pyrr_{14}]^+$ is 1-butyl-1-methylpyrrolidinium, reported as a function of formulation and select comparisons are made wherein this IL is replaced with an acyclic ammonium cation analogue IL, *N*-butyl-*N*,*N*-dimethyl-*N*-

*Electrochemical Society Member.
[z]E-mail: aneale01@qub.ac.uk; johan.jacquemin@qub.ac.uk; jj@univ-tours.fr

ethylammonium; [N_{1124}][TFSI]. Furthermore, as a function of the binary mixture formulation, electrochemical measurements were utilized to investigate electrochemical stability windows, solubilities and diffusivities of dissolved O_2 and characteristics of the electroreduction of dissolved O_2.

Experimental

Materials and syntheses.—1-Bromobutane (98%), *N*,*N*-dimethyl-*N*-ethylamine (99%), *N*-methylpyrrolidine (99%), tetraethylene glycol dimethyl ether (>99%), acetone (99.8%), dichloromethane (99.5%), diethyl ether (>99%) and ferrocene (98%) were purchased from Sigma-Aldrich. Lithium bis{(trifluoromethyl)sulfonyl}imide (battery grade) was purchased from 3 M. All reagents used for synthesis were used as received. ^{1}H and ^{13}C NMR spectra were recorded at 293.15 K on a Bruker Avance DPX spectrometer at 300 MHz and 75 MHz, respectively. Lithium content was determined by inductively coupled plasma optical emission spectroscopy (ICP-OES) on an Agilent 5100 ICP-OES. The determination of lithium content and CHNS Microanalysis were performed by Analytical Services at Queen's University Belfast. The full description of the IL synthetic procedures for [$Pyrr_{14}$][TFSI] and [N_{1124}][TFSI] is provided in the electronic supporting information (ESI) along with NMR characterization and spectra and the results of Microanalysis and lithium and water content.

Sample preparation.—Prior to any physical or electrochemical measurements, the synthesized ILs were dried in a two-step procedure. The ILs were firstly dried under vacuum (ca. 10^{-3} mbar) using a rotary-vane vacuum pump (RV3, Edwards) at elevated temperatures (363 K – 373 K) with stirring to remove the majority of water over a period of two days. Without exposing the IL sample to ambient atmosphere, these were further dried under high-vacuum (ca. 10^{-5} – 10^{-6} mbar) using a turbomolecular vacuum pump (HiCube 80 Eco, Pfeiffer Vacuum) with heating (363 – 373 K) and stirring over a further period of one or two days. The ILs were then immediately stored in an Ar-filled glove box (<2 ppm, H_2O) without exposure to external atmosphere. The water content of samples was analyzed by Karl Fischer Coulometric titration (899 Coulometer, Metrohm) where the resolution of the measurements was 0.001 wt% (or 10 ppm) and the measurements were conducted in triplicate. This drying process of the ILs was found to effectively reduce water content below 10 ppm (i.e. below the measurable range for the device).

Furthermore, prior to any physical or electrochemical measurements, the TEGDME solvent was purified by vacuum distillation over freshly activated molecular sieves (4 Å). Approximately 10% of the starting mass was discarded in the initial and final fractions and the middle fraction was collected and stored over molecular sieves (4 Å) inside the Ar filled glove box.

Binary and ternary mixtures were prepared by mass under the Ar atmosphere of the glove box using a BP 110 S balance (Sartorius, ±0.1 mg) at a temperature of ca. 305.15 K. For all binary mixtures of IL and TEGDME, both liquids were mutually miscible and a homogeneous solution was readily achieved.

Physical measurements.—The density measurements of the liquid samples were completed using a DM40 oscillating tube density meter (Mettler Toledo, $\pm 1 \times 10^{-4}$ g · cm^{-3}) in the range of 293.15–333.15 K (± 0.01 K). Prior to any measurements, the instrument was cleaned with acetone and dried with dehumidified air. The viscosity of the samples was measured using an AMVn falling/rolling ball viscometer (Anton Paar) with a 1.8 mm capillary (2.5–70 mPa · s range) in the range of 293.15–333.15 K (± 0.01 K) at atmospheric pressure.

The conductivity measurements were completed using a sensION+ EC71 benchtop meter with a 3-pole platinum sensION+ 5070 conductivity probe (<0.5% of range) with an in-built Pt1000 temperature probe (Hach Lange). The conductivity probe was calibrated using aqueous KCl standard conductivity solutions (147 μS · cm^{-1}, 1413 μS · cm^{-1}, and 12.88 mS · cm^{-1} at 298.15 K). Measurements of the binary mixture conductivity as a function of formulation were completed inside the Ar-filled glove box at ca. 305 K ± 1 K. This temperature was dictated by the internal atmosphere of the glove box. To complete these measurements a fixed mass of one component was weighed accurately into a custom-built 2 necked glass flask. A small stirrer bar was added to the bottom of the flask and the conductivity probe was inserted into the liquid sample via one glass neck and the conductivity and temperature of the pure component was recorded. Small amounts of the second component were then added directly to the liquid sample via the second neck and the mass of the addition was accurately recorded by difference. The solution was then mixed well to ensure homogeneity and the conductivity and temperature of the binary mixture was recorded, without stirring, once a stable reading was attained. This process of adding small, accurately weighed amounts of the second component and measuring conductivity and temperature was repeated continuously on the same sample to provide conductivity data for a wide range of compositions of the binary mixtures. For conductivity measurements on fixed compositions as a function of temperature, the samples were prepared inside the glove box by immersion of the conductivity probe into a glass test tube containing the liquid sample and a small magnetic stirrer. The probe was sealed inside the tube using an O-ring seal and Parafilm. The conductivities of the samples were then measured as a function of temperature within a range of 293.15–363.15 K (±0.2 K) and the sample was heated using a small oil bath. The conductivity and temperature of the sample were recorded, without stirring, once a stable reading (ca. one minute) was observed.

Computational methods.—Calculation of the IL free volume was conducted using the COSMO*thermX* software (version C30 15.01) with COSMO files computed with the DFT/B3LYP/TZVP level of theory as described by our group previously.[35,36] As demonstrated previously, an estimation of IL free volume can be straightforwardly acquired using the COSMO-RS (COnductor-like Screening MOdel for Real Solvents) computational method.[37] In short, the free volume is calculated as the difference between the molar volume (calculated using the ratio between the molecular weight and the density at 303 K predicted by the COSMO*thermX* software) and the COSMO volume of each IL. Herein the COSMO volume, i.e. the total volume encompassed by the computed COSMO surface, of the IL is the sum of COSMO volumes of each anion and cation.

Electrochemical measurements.—Electrochemical experiments where a macro working electrode is utilized were completed using a VMP3 multichannel workstation (Biologic Science Instruments). Electrochemical experiments where the working electrode was a micro-electrode were completed using either the VMP3 multichannel workstation equipped with a low-current module or an Autolab PGSTAT302 workstation (Metrohm). All electrochemical measurements were conducted in a custom-built 6 necked glass cell (two gas inlet/outlet ports and four electrode ports) designed to facilitate three-electrode electrochemical experiments with two different working electrodes in the same small volume (ca. 1–1.5 cm^3) of electrolyte solution. The gas inlet was fitted with a bubbler enabling the gas to be bubbled directly into the liquid electrolyte. The counter electrode was a Pt wire coil heat sealed into a glass capillary and the reference electrode was a Ag-wire immersed in a 0.01 mol · dm^{-3} solution of silver trifluoromethanesulfonate (Ag[OTf]) in [$Pyrr_{14}$][TFSI] separated from the bulk solution by a glass frit (herein referred to as Ag[OTf]/Ag). The macro and micro working electrodes used were a glassy-carbon macro-disk (3 mm diameter, ALS Co. Ltd.) and a Pt micro-disk electrode (10 μm diameter, Model G0225, Princeton Applied Research), respectively. Prior to any measurements the two working electrodes were polished using alumina slurries of decreasing grain size (1.0 μm, 0.3 μm and 0.05 μm, Buehler) in ultra-pure water on microcloth soft lapping pads (Kemmet Ltd.). After polishing and rinsing with ultra-pure water, the electrodes were sonicated for 2 min in ultra-pure water to remove any residual alumina. The area of the Pt micro-disk electrode was calibrated by measuring the steady-state

current of the single-electron oxidation of 2 mmol $\cdot$ dm^{-3} ferrocene in a 0.1 mol $\cdot$ dm^{-3} solution of tetrabutylammonium perchlorate in acetonitrile. In this solution, the diffusion coefficient, D, is known to be 2.3×10^{-9} m$^2 \cdot$ s^{-1} at 293.15 K,[38] (2.43×10^{-9} m$^2 \cdot$ s^{-1} at 298.15 K)[39] and is, in turn, used to calibrate the radius, r_e, of the micro-disk electrode using the equation

$$i_{ss} = 4nFDC^b r_e \quad [1]$$

where i_{ss} is the steady-state oxidation current, n is the number of electrons transferred ($n = 1$ for the oxidation of ferrocene), F is the Faraday constant (96485 C $\cdot$ mol^{-1}) and D and C^b are the diffusion coefficient and concentration of ferrocene in the bulk acetonitrile solution.

The 6-port electrochemical cell was prepared inside the Ar-filled glove box. The gas inlet and outlet ports were fitted with valves and the cell was completely sealed inside the glove box. Outside of the glove box, the sealed cell was placed inside an incubator (Genlab), holding the sample at 303 $\pm$ 1 K, which also acted as an effective Faraday cage. The gas inlet/outlet ports were connected to as gas supply via Swagelok connections. High-purity O_2 (N5.0, BOC) was flowed via two $CaSO_4$ desiccant columns (Drierite) and a small tube containing P_4O_{10} desiccant directly into the liquid electrolyte of the glass cell. Micro-disk electrode voltammetry was conducted periodically, while O_2 bubbling was paused, to determine when the solution had become saturated (typically 15–20 min). Micro-disk experiments were conducted prior to switching to the GC macro-disk electrode based on the consideration that any changes made to the electrolyte by unexpected side-reactions during voltammetry or chronoamperometry would occur on a much smaller scale (for the micro-disk) and, therefore, have less significant effect on subsequent measurements.

Once the electrolyte was deemed saturated with O_2, micro-disk electrode cyclic voltammetry (CV) was conducted in the region of 0 to -2.5 V vs. Ag[OTf]/Ag. Potential step chronoamperometry (CA) experiments at the micro-disk electrode were then conducted in the O_2 saturated electrolyte. The potential of the Pt micro-disk electrode was held at a potential of zero Faradaic current (0 V vs. Ag[OTf]/Ag) and then stepped instantaneously to a potential at which the reduction of dissolved O_2 is diffusion controlled (ca. -2.3 to -2.2 V vs Ag[OTf]/Ag; as determined from the current plateaus observed during CV experiments). The potential was held at the diffusion controlled reducing voltage for several seconds and the current was recorded with a sampling time $\leq$ 0.001 s. CA potential step experiments were repeated multiple times for each sample with a minimum period of 15 min between each individual measurement. The 15 min resting period was employed to enable the distribution of dissolved O_2 to equilibrate following the perturbation caused by the potential step, i.e. so that the concentration of dissolved O_2 local to the electrode surface can relax to equal the concentration of O_2 dissolved in the bulk electrolyte.

The resulting chronoamperometric transients were then analyzed using the Shoup and Szabo equation (Equation 2) to extract best-fit coefficients for concentration (c) and diffusion coefficient (D) of the analyte, dissolved O_2.[40] The current (i) is fitted as a function of time (t) using the equation

$$i = 4nFcDf(t) \quad [2]$$

where n is the number of electrons transferred; F is the Faraday constant (96485 C $\cdot$ mol^{-1}) and $f(t)$ is given by Equation 3:

$$f(t) = 0.7854 + 0.8862\sqrt{\frac{r_e^2}{4Dt}} + 0.2146\exp\left(-0.7823\sqrt{\frac{r_e^2}{4Dt}}\right) \quad [3]$$

where r_e is the radius of micro-disk electrode, fixed by the calibration described previously. Simulated CA transients were generated using a non-linear fitting function (OriginPro 8.1) of Equations 2 and 3 to attain a best fit with the experimental data and, therefore, to attain best-fit values for the unknown variables, $c(O_2)$ and $D(O_2)$. Transients were typically analyzed over a period of 0.02 – 2 s; the current response within the first 20 ms is considered to be highly dependent on rapid non-faradaic charging of the electrical double layer and is, therefore, not included in the analysis.

Following the CA experiments at the Pt micro-disk electrode, the working electrode was changed to the GC macro-disk electrode. Cyclic voltammetry was conducted within a voltage range of 0 to -2 V vs. Ag[OTf]/Ag at a range of scan rates. A period of approximately 5–8 min was utilized between each scan to allow the system to equilibrate. All CV experiments conducted at the GC electrode were completed with *iR*-compensation based on the ZIR-technique at 85% within the EC-Lab software (Biologic Science Instruments).

Following all CA and CV experiments at both working electrodes, a small mass of ferrocene was added into the liquid electrolyte. CV experiments at both electrodes were used to determine an estimation of the formal redox potential of the single electron oxidation of ferrocene to ferrocenium. The formal redox potential is utilized as an internal reference couple to normalize the measured potential at the Ag[OTf]/Ag reference electrode versus the Fc^+/Fc potential.

Results and Discussion

Physical characteristics of electrolyte blends.—As discussed previously, a primary disadvantage typically associated with ILs for electrochemical energy storage systems relates to the sluggish transport properties commonly observed. High viscosities and moderate-to-poor conductivities exhibited by the ILs, which generally worsen upon the addition of Li-salts, inhibit the mobility of active species involved in charge/discharge processes and contribute to increased resistances. These factors are among the primary motivations for blending the IL component with a lower viscosity molecular solvent. The effect of formulation on the physical and electrochemical properties is described for the full range (i.e. from $X = 0$ to 1) for the (X)[Pyrr$_{14}$][TFSI] – (1-X)TEGDME binary mixtures. For comparison of structural effects, characterization of an acyclic cation analogue IL, [N$_{1124}$][TFSI] and the respective $x_{IL} = 0.4$ binary mixture with the TEGDME solvent, is also described. As is evidenced from the following discussion, despite being one carbon atom lighter than the cyclic IL, the transport properties of both ILs are very similar, allowing for good comparison of structural effects.

The measurements of viscosity of the binary mixture (X)IL–(1-X)TEGDME were completed using a rolling ball viscometer as a function of the molar fraction of the IL component and temperature and the results are presented in Figure 1a. The numerical data is given in Tables S1 and S2 in the ESI for the [Pyrr$_{14}$][TFSI] and [N$_{1124}$][TFSI] mixtures, respectively.

Firstly, the measured viscosities of the neat [Pyrr$_{14}$][TFSI] (77.7 mPa $\cdot$ s at 298.15 K) and neat TEGDME (3.3 mPa $\cdot$ s at 298.15 K) are in good agreement with values previously reported in the literature.[41–43] As would be expected, the viscosity of all studied mixtures is reduced with increased temperature. Furthermore, across all temperature ranges, continued addition of TEGDME to the IL affects a reduction in the measured viscosities wherein the greatest reduction in viscosity is observed at lower temperatures; i.e. the viscosities of the mixtures converge at higher temperatures.

An additional benefit of mixing ionic liquids with lower viscosity molecular solvents is related to the promotion of electrolytic conductivity typically observed. Relatively strong prevalent Coulombic interaction between the counterions within the IL ultimately limit the ionic mobility and, in turn, the ability of the IL to rapidly conduct charge. Presented in Figure 1b is the measured conductivity of the binary mixture (X)[Pyrr$_{14}$][TFSI] – (1-X)TEGDME as a function of IL molar fraction, X[Pyrr$_{14}$][TFSI]. The measurement was completed under an inert, dry atmosphere of an Ar-filled glove box by periodically adding small, accurately weighed quantities of one component to a fixed mass of the second component. After each addition, the mixture is effectively mixed and the conductivity is recorded. The temperature of these measurements is 305 K $\pm$ 1 K, as dictated by the internal atmosphere of the glove box. Within IL systems, the observed bulk viscosity and conductivity are typically inversely linked. As such, in agreement with the aforementioned reduction in viscosity, the measured conductivity is increased upon addition of TEGDME. This observation primarily relates to the increased mobility of the

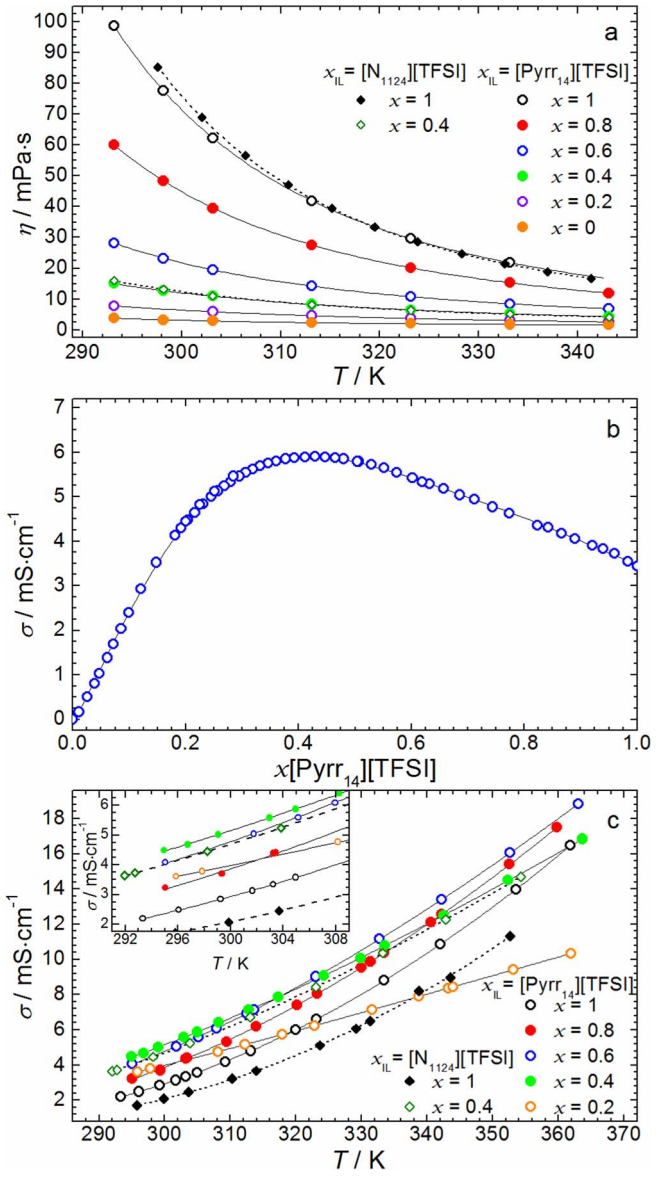

Figure 1. (a) Measured viscosity of the (*X*)IL – (1-*X*)TEGDME binary mixtures as a function of temperature. (b) Conductivity of the (*X*)[$Pyrr_{14}$][TFSI] – (1-*X*)TEGDME binary mixture as a function of a semi-continuous range of formulations at a single isotherm of 305 ± 1 K. (c) Conductivity of a set of discreet formulations of the (*X*)IL – (1-*X*)TEGDME binary mixture as a function of temperature. The inset graph represents a zoomed in section of the data at lower temperatures. The circle and diamond symbols represent data for the [$Pyrr_{14}$][TFSI] and [N_{1124}][TFSI] based mixtures, respectively. Solid and dashed lines (a and c) represent VTF correlation of the [$Pyrr_{14}$][TFSI] and [N_{1124}][TFSI] based mixtures, respectively.

constituent ions within the electrolyte binary mixture. However, upon further addition of TEGDME, a maximum conductivity (5.9 $mS \cdot cm^{-1}$) is observed at x[$Pyrr_{14}$][TFSI] = 0.43. Beyond this molar fraction, while the added TEGDME promotes further reductions in viscosity (and an inferred increase in the mobility of ionic species), this factor is balanced by a dilution effect and, as the number of ions further reduces, so too does the measured electrolytic conductivity. Incidentally, the position of this maximum is the reason for selecting the x = 0.4 binary mixture for the [N_{1124}][TFSI]/TEGDME blend as a comparative binary mixture.

Utilizing the measurements of the density of the mixtures (raw numerical data presented in Table S3 in the ESI), the concentration of [$Pyrr_{14}$][TFSI] in TEGDME was calculated across the full formulation range. The conductivity is plotted as a function of IL concentration in Figure S5 in the ESI. The conductivity maximum, observed at *X*[$Pyrr_{14}$][TFSI] = 0.43 corresponds to a concentration of ca. 1.66 $mol \cdot dm^{-3}$. Although the vapor pressure of both components of the binary mixture are known to be very low (0.132 kPa at 373 K for TEGDME),[44] having a higher ionic component within the formulation can effectively lower the vapor pressure of the mixture (according to Raoult's Law). This consideration is important for the improvement of electrolyte safety by reducing the likelihood of forming combustible vapors in the event of device malfunction.

The temperature dependence of the conductivity was also measured for discrete formulations of the binary mixture, presented in Figure 1c. The numerical conductivity data as a function of formulation and temperature is provided in Tables S4 and S5 in the ESI for the [$Pyrr_{14}$][TFSI] and [N_{1124}][TFSI] mixtures, respectively. As expected, increasing the sample temperature results in an increase in the observed conductivity relating to the increased mobility of the charge carrying ions. The inset graph in Figure 1c, representing a zoomed in plot of the lower end of the temperature scale, demonstrates that the same trend in conductivity as function of IL molar fraction is observed compared to the data presented in Figure 1b. Across the temperature range, the shapes of the curves highlight a change in behavior as the quantity of IL in the mixture decreases. The temperature dependence of the solvent rich formulation, wherein $X = 0.2$, is almost linear across the studied range while the formulations containing higher IL fractions increase more exponentially. As a result, at higher temperatures there is a shift in the observed maximum conductivity toward more IL rich formulations. This is related to the competition between the mobility of the charge carrying ionic species (which increases with temperature and at greater TEGDME fractions) and the concentration of these ions available to conduct the charge. As such, at higher temperatures, the mobility of the ionic constituents in the IL rich formulations becomes sufficiently high (as inferred from the significant reduction in viscosities) that high ionic concentrations remain beneficial. This shift in the observed maxima is shown graphically in Figure S6 in the ESI. Additionally, further extrapolation of the observed temperature dependencies (using the Vogel-Tammann-Fulcher equation, discussed below) would suggest that, under a purely hypothetical scenario without the inevitable evaporation of the molecular solvent, at temperatures greater than ca. 420 K, the neat IL would exhibit the greatest conductivity. In this hypothetical scenario, the mobility of the charge carrying species (i.e. all components of the liquid) becomes sufficiently high so that addition of this solvent only serves to dilute the ions and, in turn, reduce the electrolytic conductivity.

The experimental viscosity, η, and conductivity, σ, of the mixtures were correlated as a function of the temperature, *T*, using the Vogel-Tammann-Fulcher (VTF) equations

$$\eta = \eta_o exp\left(\frac{B^{\eta}}{T - T_o^{\eta}}\right) \quad [4]$$

$$\sigma = \sigma_o exp\left(\frac{-B^{\sigma}}{T - T_o^{\sigma}}\right) \quad [5]$$

where η_o and σ_o represent the limiting viscosity and limiting conductivity, respectively, and B^{η}/ B^{σ} and $T_o{}^{\eta}/T_o{}^{\sigma}$ are correlation parameters relating to the pseudo activation energies and the glass transition temperatures of the mixtures, respectively. Excellent correlation is achieved for all data sets as a function of temperature allowing for accurate interpolation of properties at specific temperatures. The coefficients of the best-fits for the VTF equations for all mixtures are given in Tables S1 and S2 for viscosity and Tables S4 and S5 conductivity in the ESI.

The relationship between viscosity and conductivity in ILs is commonly inspected in terms of ionicity by plotting a variation of the Walden plot; a plot of $Log_{10}(\eta^{-1})$ vs. $Log_{10}(\Lambda)$ where η^{-1} and Λ represent the reciprocal viscosity (or fluidity, in units of $Poise^{-1}$) and the molar conductivity (in units of $S \cdot cm^2 \cdot mol^{-1}$), respectively. The molar conductivity, Λ, is calculated from the specific conductivity, σ,

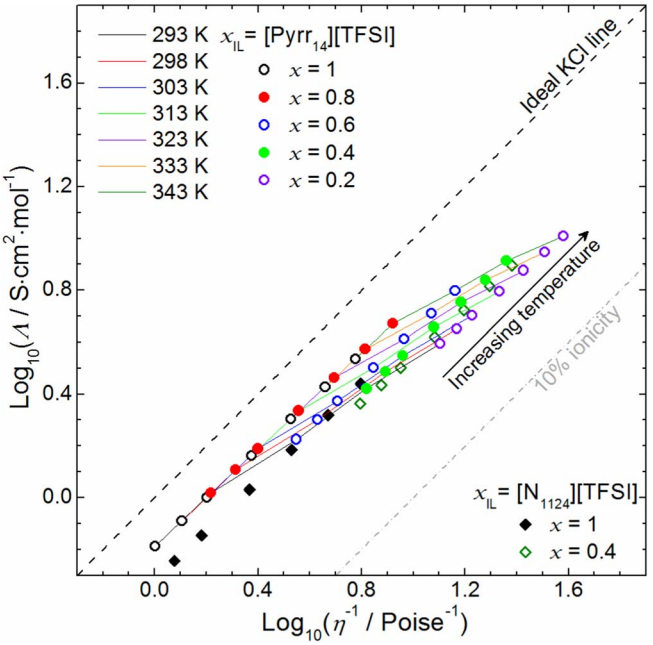

Figure 2. Walden plot of the (*X*)IL – (1-*X*)TEGDME binary mixtures as a function of the temperature and composition. The different symbols represent individual compositions within a range of temperatures while the solid connecting lines represent the isothermal behavior as a function of composition. The dashed line and dash-dot line represent the so-called ideal KCl line and a % ionicity of 10%, respectively. The circle and diamond symbols represent data for the [Pyrr$_{14}$][TFSI] and [N$_{1124}$][TFSI] based mixtures, respectively.

and IL concentration, c_{IL},

$$\Lambda = \frac{\sigma}{c_{IL}} = \frac{\sigma \cdot M_r}{w_{IL} \cdot \rho} \quad [6]$$

where M_r is the molecular weight of the IL (422.4 g · mol^{-1} and 410.4 g · mol^{-1} for [Pyrr$_{14}$][TFSI] and [N$_{1124}$][TFSI], respectively) and w_{IL} and ρ represent the mass fraction of the IL and the density of the mixture, respectively. The experimental density for the two [N$_{1124}$][TFSI] based electrolytes is shown as function of temperature in Table S6 in the ESI. The Walden plots for the (*X*)[Pyrr$_{14}$][TFSI] – (1-*X*)TEGDME binary mixtures given presented both as a function of formulation and temperature are shown in Figure 2. The dashed $y = x$ line represents the idealized Walden behavior of a 0.01 mol · dm^{-3} aqueous solution of KCl in which the ionic species of the strong electrolyte are considered to be fully dissociated and both cation and anion exhibit similar mobilities.[45,46]

Deviations below this line within IL systems are typically attributed to a tendency of the IL to form ion-ion pairs and the magnitude of such deviation is indicative of the strength of these interactions. Ionic association in the electrolytes reduces availability of the ions to conduct the charge in the liquid and, therefore, the observed molar conductivity is not as a high as may be expected for a given IL fluidity according to the Walden rule. The degree of disassociation may be inferred from the Walden product, *W*,

$$W = \Lambda\eta \quad [7]$$

wherein any point on the ideal KCl line would equal 1 (Poise · S · cm^2 · mol^{-1}) representing 100% dissociation. Furthermore, the Walden product of any point below the ideal line represents a decimal expression of the percentage dissociation, or percentage ionicity.

However, as has been described previously,[47] and is true for the (*X*)IL – (1-*X*)TEGDME binary mixtures presented in this work, the slope of the of Walden behavior with respect to temperature quite commonly is not equal to 1. In fact, the gradient of the reported binary mixtures ranges from 0.868 to 0.948 and the respective Walden product is temperature dependent for each mixture. An alternative approach involves the utilization of the fractional Walden rule wherein an additional exponent, α, is introduced

$$W^f = \Lambda\eta^\alpha \quad [8]$$

$$Log_{10}(\Lambda) = Log_{10}\left(W^f\right) + \alpha \cdot Log_{10}\left(\eta^{-1}\right) \quad [9]$$

where W^f represents the fractional Walden product. Linear regression of the fractional Walden behavior of each binary mixture yielded excellent correlation based on Equation 9. The resulting gradients (α), intercepts (Log$_{10}$(W^f)), coefficients of determination, R^2, and the calculated percentage ionicity, % ionicity, are shown for each binary composition in Table I. The % ionicity, or degree of dissociation, of the neat [Pyrr$_{14}$][TFSI] is in very good agreement values available in the literature,[42] wherein the majority of constituent ions are available for conduction and, as such, is considered a so-called '*good ionic liquid*'.[45] Comparatively, the apparent ionicity of the analogous acyclic IL is significantly lower in its neat form. This is indicative of a stronger tendency to form ion pairs in the [N$_{1124}$][TFSI], showing that despite the two ILs exhibiting similar viscosities, a greater proportion of the ions remain unavailable for electrolytic conduction (as shown in Figure 1c).

Table I. Linear fitting parameters, and the resulting calculated percentage ionicity, from the fractional Walden rule (Equation 8/9) of the different compositions of the (*X*)IL – (1-*X*)TEGDME binary mixtures.

X_{IL}	% ionicity	Log$_{10}$(W^f / S · cm^2 · mol^{-1})	α	R^2
		[Pyrr$_{14}$][TFSI]		
1	64.5	−0.190	0.936	1.00000
0.8	65.6	−0.183	0.923	0.99998
0.6	51.7	−0.286	0.933	0.99999
0.4	47.2	−0.326	0.912	1.00000
0.2	43.4	−0.363	0.868	0.99996
		[N$_{1124}$][TFSI]		
1	48.2	−0.317	0.948	0.99999
0.4	43.7	−0.360	0.907	0.99986

Upon addition of a small quantity of solvent to [Pyrr$_{14}$][TFSI], i.e. where $X = 0.8$, a small but not significant increase in the % ionicity is observed. However, at more solvent-rich formulations, the apparent degree of dissociation drops, indicating the promotion in the measured conductivity is not as a high as expected given the observed reduction in electrolyte viscosity. This observation, while also holding true for the $X = 0.4$ [N$_{1124}$][TFSI] binary mixture, is contrary to the behavior of traditional electrolytes, wherein the solvent is expected to promote the dissociation of constituent ions by solvation. However, this behavior has been reported previously for [TFSI]$^-$ based ILs in binary mixtures with solvents possessing both high and low dielectric constants.[46,48–50] The results suggest the presence of the solvent promotes ionic aggregation or the formation of ion pairs within the liquid. Such observations have permitted the speculation of non-homogeneity within the mixture by the formation of microphases wherein the ionic liquid structure is retained upon dilution.[46]

To qualitatively probe the interactions between the two components, the excess molar volume, $V_m{}^E$, of the mixtures was calculated using the following series of equations

$$V_m^E = V_m^r - V_m^i \quad [10]$$

where $V_m{}^r$ and $V_m{}^i$ represent the experimental molar volume and ideal molar volume, respectively, as a calculated by

$$V_m^r = \left(\frac{x_1M_1 + x_2M_2}{\rho_{exp}}\right) \quad [11]$$

$$V_m^i = \left(\frac{x_1M_1}{\rho_1}\right) + \left(\frac{x_2M_2}{\rho_2}\right) \quad [12]$$

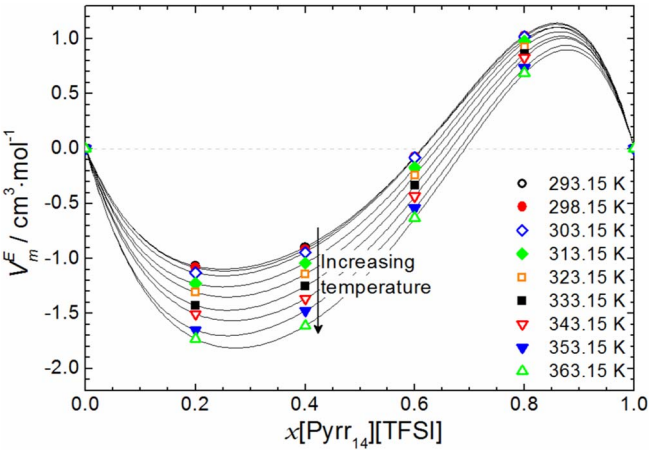

Figure 3. Excess molar volumes of the (*X*)[Pyrr$_{14}$][TFSI] – (1-*X*)TEGDME binary mixtures over the temperature range of 293.15–363.15 K. The solid lines represent the calculated correlation by the Redlich-Kister expansion using Equation 13 with parameters reported in Table S7 in the ESI.

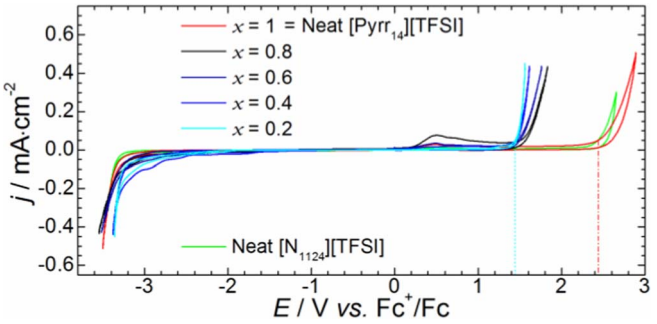

Figure 4. Electrochemical stability window of the (*X*)[Pyrr$_{14}$][TFSI] – (1-*X*)TEGDME binary mixtures at a glassy carbon macro-disk working electrode. All cycles were completed at a scan rate of 2 mV · s^{-1}. The electrochemical stability window of the pure acyclic alkylammonium IL, [N$_{1124}$][TFSI], is also shown.

where x_i and M_i are the molar fraction and molecular weight of components 1 and 2, respectively, ρ_{exp} is the experimentally measured density of the mixture and ρ_i is the density of the pure components 1 and 2. The calculated V_m^E values for the (*X*)[Pyrr$_{14}$][TFSI] – (1-*X*)TEGDME are presented for a range of temperatures as a function of the composition in Figure 3. The solid lines represent correlation of the data by a third order Redlich-Kister polynomial expansion

$$V^E_{m,calc} = x_1 x_2 \sum_{k=0}^{3} A_k (x_1 - x_2)^k \qquad [13]$$

where A_k is the coefficient of the polynomial expansion of the order k. The coefficients of the Redlich-Kister correlation are presented in Table S7 in the ESI along with the standard deviation, σ_{SD}, as calculated by the equation

$$\sigma_{SD} = \left[\frac{\sum \left(V^E_{m,Exp} - V^E_{m,Calc} \right)^2}{n - p} \right]^{0.5} \qquad [14]$$

where $V_m{}^E{}_{Exp}$ represents the experimentally determined excess molar volumes, $V_m{}^E{}_{Calc}$ represents the excess molar volume as calculated by Equation 13, and n and p represent the number of experimental data points and the number of coefficients used in the correlation, respectively.

The sign and magnitude of deviations in molar volumes shift as a function of the composition. In general, deviations from ideal V_m^E may be caused by cohesive or repulsive intermolecular interactions between the components of the mixture and/or by reorganization of the molecular packing within the solution depending on size and shape contributions. The sign of the V_m^E of the (*X*)[Pyrr$_{14}$][TFSI] – (1-*X*)TEGDME binary mixtures takes the form of a S-shaped curve wherein the value is positive in IL rich formulations and shifts to larger, negative deviations in the solvent rich formulations. Furthermore, across the entire composition range the calculated excess molar volumes decrease (i.e. become more negative) with increasing temperature. In addition, the calculated excess molar volume for the $X = 0.4$ [N$_{1124}$][TFSI] mixture corresponds to slightly larger negative deviations (ca. -1.67 cm^3 · mol^{-1} at 298.15 K), albeit of a similar magnitude to the equivalent [Pyrr$_{14}$][TFSI] formulation.

Positive deviations in the IL rich compositions of the studied mixtures are indicative of expansion of the occupied volume relative to the molar volumes of the pure components. This could be attributed to the disruption of associative forces between constituent ions of the IL or the result of inefficient packing of the reasonably long chain oligoether in the IL structure. Conversely, upon further dilution with TEGDME the excess molar volume shifts to larger negative deviations indicative of contraction of the molar volumes. With [TFSI]$^-$-based salts paired with small, charge dense alkali metal cations (i.e. Li$^+$ ions), the long flexible glyme chains are able to effectively coordinate the positive charge via the ethereal oxygen lone pairs. However, in mixtures with a bulky organic, more sterically hindered, weak Lewis acidic pyrrolidinium cation, any such interaction would be expected to be weaker and significantly more complex. In the TEGDME rich formulations (wherein $X_{IL} = 0.4, 0.2$) significant drops in the % ionicity (Table I, Figure 2) are indicative of a reduction in the proportion of *free* ions available for the conduction of charge. This observation could be supported by the strong, negative deviations in V_m^E shown in Figure 3. In the binary mixtures, the oxygen atoms in the glyme solvent chain will preferentially exist closer to areas of partial positive charge on the cation (in competition with the anion). For both cations, the reasonably distributed positive charge lies most accessibly on the alpha hydrogens of the four methyl/methylene carbons surrounding the nitrogen heteroatom center. As the quantity of TEGDME increases to equal and exceed a 1:1 mole ratio, the TEGDME may preferentially occupy the majority of these partially positive sites and, hence, restrict the available positioning of the negatively coordinating sulfonyl oxygens of the [TFSI]$^-$ anion within the first shell surrounding the IL cation. In effect, this spatial restriction may increase the probability of ion pair formation within the solvation core shell.

Electrochemical measurements of IL/TEGDME blends.—One attractive feature commonly exhibited by ILs is their wide electrochemical stability windows. Defined by the potential range between the cathodic and anodic potential limits of bulk reductive and oxidative decomposition of the electrolyte, respectively, large electrochemical stability windows have enabled access to previously inaccessible voltage ranges in electroanalytical and electrodeposition techniques.[51] For electrochemical energy storage devices, the wide electrochemical window provides an electrochemically unreactive medium for supporting the electroactive faradaic processes in battery technologies and the electrostatic charge separation which underpins the energy storage mechanism in EDLCs. Given the direct proportionality between EDLC energy and power densities and the square of the cell operative voltage,[52] increasing the stable voltage ranges of the materials is one of the main attractions of utilizing highly electrochemically stable ILs in this field. The electrochemical window of the studied IL/TEGDME mixtures was measured by cyclic voltammetry (CV) at a glassy carbon macro-disk working electrode (3 mm diameter) under an inert, dry atmosphere of an Ar-filled glove box. The CVs of the studied mixtures are shown in Figure 4. The onset potentials for reductive decomposition (E_c) and oxidative decomposition (E_a) of the electrolyte are approximated by a graphical method to estimate the potential at which a tangent to the main oxidation/reduction wall crosses the *flat* electrochemical baseline wherein no significant faradaic current is observed. The magnitude of the electrochemical stability windows, ΔE (defined by the equation

$\Delta E = E_a - E_c$) of the two ILs, [Pyrr$_{14}$][TFSI and [N$_{1124}$][TFSI], are almost identical at ca. (5.8–5.9) V. However, upon addition of the TEGDME solvent to the mixture, a significant reduction in the apparent anodic stability (ca. 1 V) of the electrolyte is observed irrespective of the solvent quantity. As such, while the onset potential for electrolyte oxidation increases by several tens of millivolts with increased IL proportions, the anodic potential limit of the electrolyte mixtures is limited by the TEGDME solvent. This potential limit for the oxidative decomposition of TEGDME, 1.4–1.5 V vs. Fc^+/Fc, is in good agreement with previously reported values (i.e. $E_a = 4.7$–4.9 V vs. Li^+/Li based on the experimental approximation of $E(Fc^+/Fc) = 3.25$ V vs. $E(Li^+/Li)$ in this medium).[53]

An investigation of the effect of binary mixture formulation of the transport, solubility, and electrochemistry of dissolved O_2 was conducted using voltammetric techniques at macro- and micro-disk electrodes in tandem. This has potentially interesting outcomes for the application of these formulations as IL-based electrolytes for amperometric O_2 sensors and non-aqueous metal-air batteries. Firstly, the solubility, $c(O_2)$, and diffusion coefficient, $D(O_2)$, of oxygen dissolved in the electrolyte formulations was investigated at a 10 μm diameter platinum micro-disk electrode. The electrolyte was saturated with a bubbling stream of dry O_2 gas and electrochemical measurements were completed under a sealed, static environment at 303 ± 1 K. Cyclic voltammetry (CV) was first utilized to observed the O_2 reduction/oxidation and, consequently, determine the potential step for subsequent chronoamperometry (CA) experiments. The measured CV and CA traces for the (*X*)[Pyrr$_{14}$][TFSI] – (1-*X*)TEGDME mixtures are shown in Figure 5. Additionally, the electrochemical measurements were completed using the analogous acyclic ammonium based IL, [N$_{1124}$][TFSI], and the (0.4)[N$_{1124}$][TFSI] – (0.6)TEGDME binary mixture (corresponding to the approximate formulation giving the maximum conductivity in the [Pyrr$_{14}$][TFSI] mixtures).

For oxygen reduction in both neat ILs, a typical steady-state plateau is observed on the negative going sweep of cyclic voltammetry associated with quasi-hemi-spherical type diffusion for the single-electron reduction of O_2 to $O_2^{\bullet-}$ (superoxide radical anion) at the micro-disk electrode. On the reverse sweep, both ILs show evidence of a transient type peak for the re-oxidation of the superoxide which can be ascribed to the very slow diffusion of the radical anion leading to planar-type diffusion contributions at the electrode surface. This asymmetry in the apparent mobility of the uncharged O_2 and charged $O_2^{\bullet-}$ has been reported previously,[36,54] and is presumably due to significant interactions between the negatively charged superoxide anion and the positively charged cation of the IL. Upon dilution with the TEGDME, the magnitude of the reduction current plateau is found to increase while the transient oxidation peak tends to reduce. This is likely due to the increased diffusivities of all species within the mixture as a consequence of the reduced viscosities.

An exemplary CA transient, and the respective simulated transient, is shown in Figures 5c and 5d for each of the binary mixtures. The potential step for each measurement was in the range of −2.2 to −2.3 V vs. Ag[OTf]/Ag over a period of 2 s. The solubility and diffusion coefficient of dissolved O_2 ($c(O_2)$ and $D(O_2)$, respectively), derived from correlation of CA transients using Equation 2, is shown as a function of the binary mixture formulation in Figure 6a. The numerical values are presented in Table S8 in the ESI. The O_2 solubility in neat [Pyrr$_{14}$][TFSI] (10.21 mmol · dm^{-3}) is in reasonable agreement with our previously reported value under slightly different conditions (9.15 mmol · dm^{-3} at 297 K).[36] The acyclic IL, [N$_{1124}$][TFSI], exhibits a slightly reduced solubility (8.09 mmol · dm^{-3}) compared to

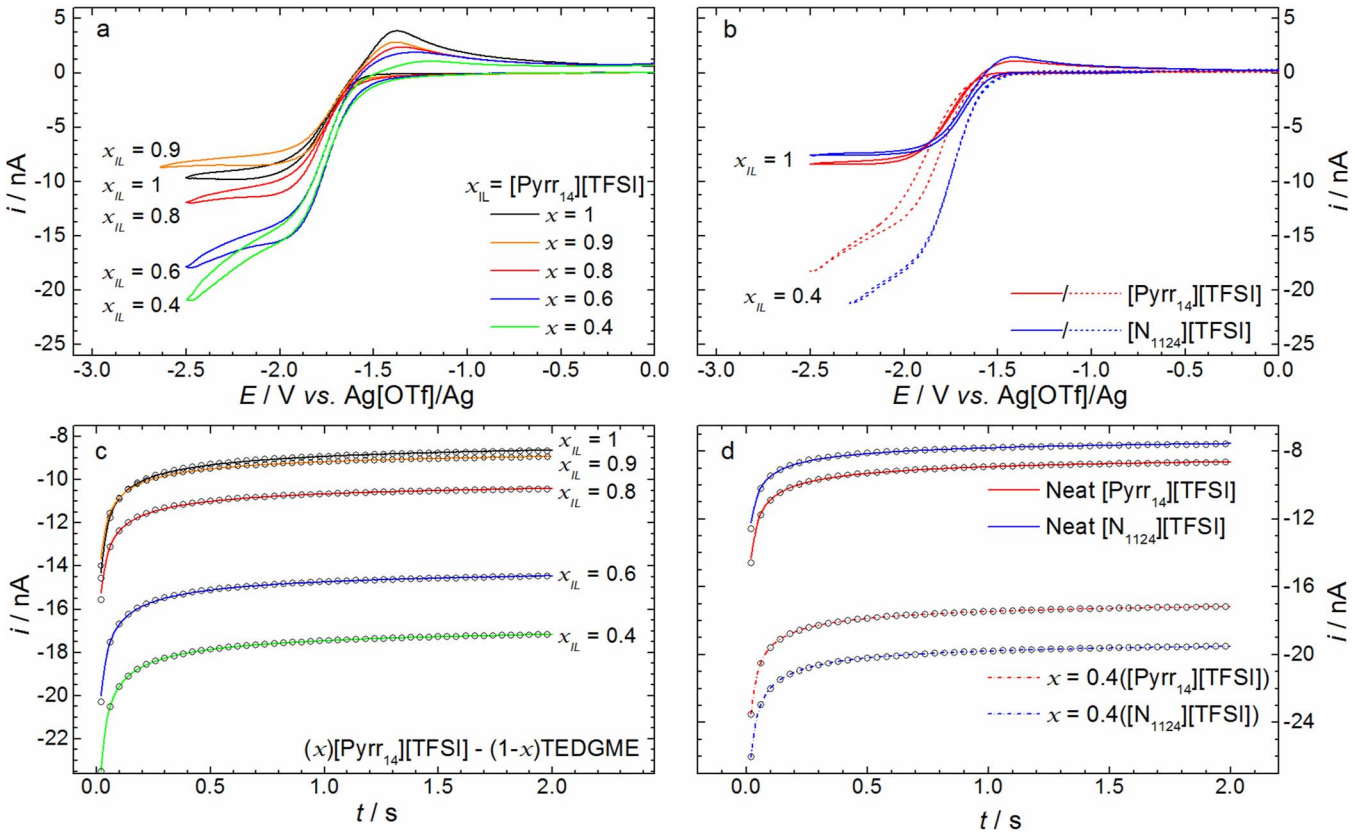

Figure 5. Electrochemical measurements of the O_2-saturated (*X*)[Pyrr$_{14}$][TFSI] – (1-*X*)TEGDME binary mixtures and the [N$_{1124}$][TFSI] IL and (0.4)[N$_{1124}$][TFSI] – (0.6)TEGDME binary mixture at a 10 μm diameter Pt micro-disk electrode at 303 ± 1 K: (a and b) Cyclic voltammograms using a scan rate of 1 V · s^{-1}; (c and d) Chronoamperometric transients for the diffusion-controlled O_2 reduction potential step. Solid lines (in c and d) represent the experimental current measurements and the overlaid circles represent the transients as simulated by the Shoup and Szabo equation (Equations 2 and 3).

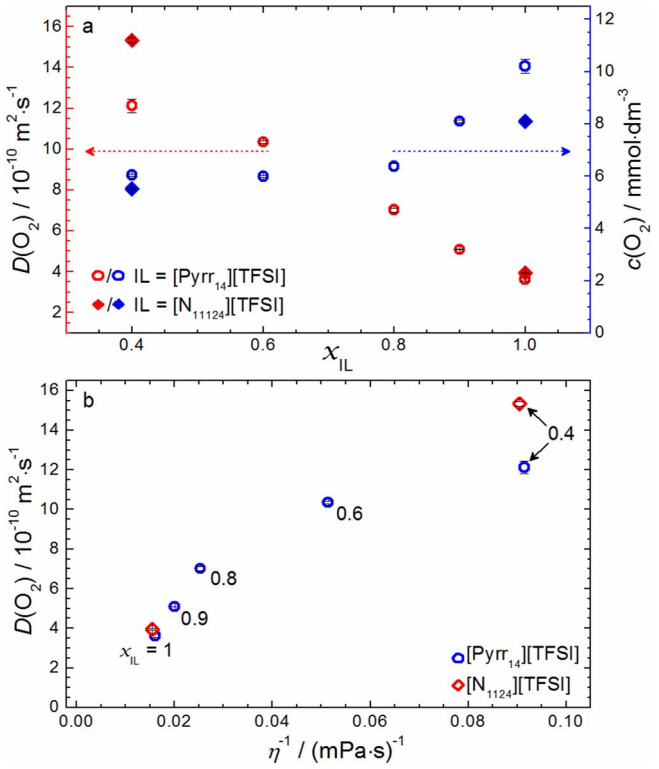

Figure 6. (a) Solubilities, $c(O_2)$, and diffusion coefficients, $D(O_2)$, of dissolved oxygen in the series of (X)IL – (1-X)TEGDME binary mixtures at 303 ± 1 K as a function of the formulation. (b) $D(O_2)$ as a function of the mixture fluidity (i.e. reciprocal viscosity, η^{-1}) of the studied binary mixtures. The numerical values in (b) highlight the molar fraction of the IL in the respective binary mixture.

its cyclic analogue. However, dilution of both ILs with the TEGDME solvent yields reduction in the uptake of dissolved O_2. This behavior is expected considering the lower solubility of O_2 in pure TEGDME; reported previously, using non-electrochemical measurements, as 4.43 mmol · dm^{-3} at 298 K.[55] Nevertheless, more interesting is the seemingly steep drop in O_2 solubility moving from $x_{IL} = 1$ to 0.9/0.8 which appears to level out at higher TEGDME fractions; indicating that even small quantities of the solvent reduce the desirable *higher* solubility in the pure IL. Considering the highly structured nature of many ILs,[56,57] the TEGDME may be affecting disruptions in the IL structure and potentially removing free holes in which the small O_2 molecule could occupy.

With regards to the transport of the dissolved gas, the O_2 diffusivity is, as expected, lowest in the two neat ILs (i.e. the most viscous media). Dilution of the ILs with the TEGDME solvents yields significant promotions in the mobility of O_2. Since viscosity is a measure of the materials resistance to flow, a logical inverse proportionality generally exists between the transport rate of solutes and the electrolyte viscosity. This relationship, i.e. $D \propto \eta^{-1}$, where η^{-1} (the reciprocal viscosity) is known as the fluidity, is commonly discussed in terms of some variation of the Stokes-Einstein equation

$$D = \frac{k_B T}{6\pi\alpha\eta} \quad [15]$$

where k_B, T and α represent the Boltzmann constant, the temperature, and the hydrodynamic radius of the solute in question, respectively. We recently reported that within a family of closely related cyclic alkylammonium [TFSI]$^-$ based (including [Pyrr$_{14}$][TFSI]), such a relationship is followed to a degree.[36] Conversely, where a significant variety of IL structures are used, Einstein-Stokes type dependencies are typically not observed for O_2, and other small solute molecules like H_2 and H_2S, suggesting that alternate solvent-solute interactions play an important role.[54] Additionally, a lower dependence on the IL viscosity may be expected for a non-coordinating solute like O_2, given the order of magnitude difference between measured values for $D(O_2)$ and the previously reported self-diffusion coefficients for pure [Pyrr$_{14}$][TFSI] (where $D([Pyrr_{14}]^+)$ and $D([TFSI]^-) = 0.25 \times 10^{-10}$ and 0.2×10^{-10} m^2 · s^{-1}, respectively, at 305 K).[58] This relationship is explored for the IL/TEGDME binary mixtures in Figure 6b. For the [Pyrr$_{14}$][TFSI]-based mixtures studied as a function of formulation, this relationship is non-linear across the studied range and, thus, inadequately described by Equation 15. Incidentally, the self-diffusion coefficient of neat TEGDME solvent at 303 K is 2–3 × 10^{-10} m^2 · s^{-1}.[59] Though the diffusivity of the O_2 analyte cannot be measured using these electrochemical techniques in a *neat* (and, therefore, electronically insulating) organic solvent, approximate extrapolation of the trend shown in Figure 6a for the [Pyrr$_{14}$][TFSI]/TEGDME mixture would suggest this value (i.e. $D(O_2)$ in neat TEGDME) would lie in the range of 13–16 × 10^{-10} m^2 · s^{-1}. Again, this is nearly an order of magnitude higher than the solvent molecule owing to the non-associative nature of neutral O_2 in TEGDME.

Interestingly, despite exhibiting lower O_2 solubilities and slightly higher viscosities at both $X = 1$ and 0.4 than the equivalent [Pyrr$_{14}$][TFSI] electrolytes, the [N$_{1124}$][TFSI] based electrolytes affords improved O_2 transport compared to the cyclic cation analogue. For the two neat ILs, the measured diffusion coefficients of the dissolved gas are within approximate experimental error but the higher O_2 solubility in [Pyrr$_{14}$][TFSI] may be related to the higher free volume (V_f) within this IL (where V_f = 41.38 cm^3 · mol^{-1} and 40.42 cm^3 · mol^{-1} at 303 K for [Pyrr$_{14}$][TFSI] and [N$_{1124}$][TFSI], respectively, as calculated using the COSMO-RS computational method). This would allow a greater quantity of cavities or holes within [Pyrr$_{14}$][TFSI] which the small neutral O_2 molecule can occupy. Within the two blended electrolytes, the O_2 solubility/diffusivity will be affected by IL-solvent interactions. As previously discussed in the concluding paragraph of the Physical characteristics of electrolyte blends section, solvent coordination with the partially positive alpha hydrogens of each cation may consequently restrict the available sites for cation-anion interaction within the first shell surrounding IL cations. This, in turn, can increase the tendency for the formation of ion-pairs. This affect appears most significant for the [N$_{1124}$][TFSI] mixture based on the lower apparent ionicity (Figure 2, Table I) and the greater reduction of V_m^E (Figure 3) relative to [Pyrr$_{14}$][TFSI]. The nature of the pyrrolidinium ring constrains the location of these two methylene carbons creating a preferred site for anion interaction,[60] increasing the probability of TEGDME coordination with the -CH$_2$- or -CH$_3$ groups of the butyl and methyl groups, respectively. The acyclic [N$_{1124}$][TFSI], however, is not constrained by a ring structure and, therefore, TEGDME-cation interaction may more readily occur at any of the four alpha hydrogen sites, allowing more effective solvation of the complete ion pair in this case. The resulting lower ionicity of the [N$_{1124}$][TFSI] will reduce probability of IL-O_2 interactions and, it is speculated that, this allows greater mobility of the dissolved gas within the TEGDME rich pockets of these apparently non-homogenous mixtures. Further investigations, however, of the structural ordering and interactions in these IL-solvent mixtures are needed.

Following completion of micro-electrode measurements, the working electrode connection was moved to the glassy carbon macro-disk electrode where CV experiments were performed on the equivalent O_2-saturated binary mixtures. The respective voltammograms for these mixtures are shown in Figures 7a and 7b. Multiple scan rates (v) were utilized between 5 and 500 mV · s^{-1} within a voltage window of 0 to −2 V vs. Ag[OTf]/Ag. A summary of the peak potentials, E_{pc} and E_{pa}, peak current densities, j_{pc} and j_{pa}, and peak charges, Q_c and Q_a (where subscript c or a refers to cathodic or anodic processes, respectively) for the 20 mV · s^{-1} scans is shown in Table II. For the neat ILs, charge and current ratios for the redox processes exist very close to unity at these modest scan rates while these ratios are found to decrease by 10% and more at scan rates of 100 mV · s^{-1} and greater. While this is a good indication of good

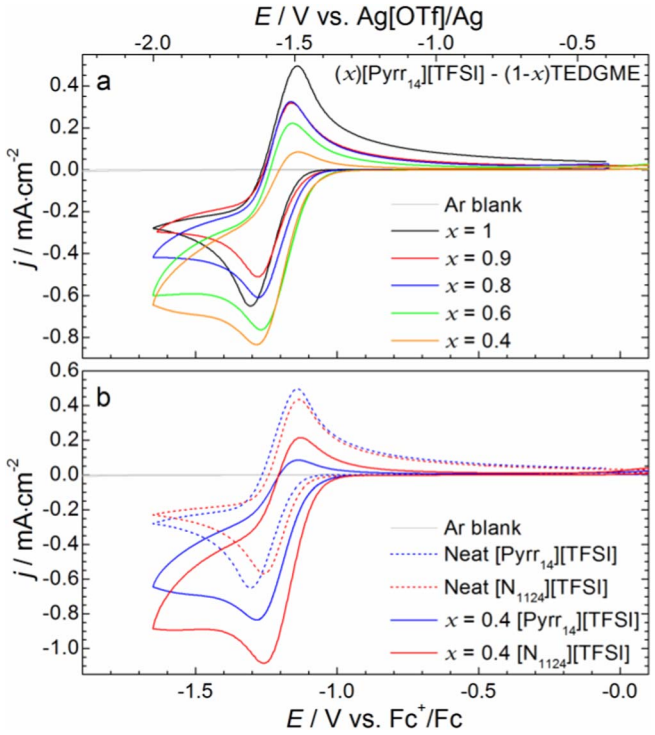

Figure 7. iR-compensated cyclic voltammograms of O_2-saturated (a) (*X*)[$Pyrr_{14}$][TFSI] – (1-*X*)TEGDME binary mixtures and (b) the [N_{1124}][TFSI] IL and (0.4)[N_{1124}][TFSI] – TEGDME binary mixtures at a 3 mm diameter glassy carbon macro-disk electrode at 303 ± 1 K. All cycles were completed at a scan rate of 20 mV · s^{-1}.

chemical reversibility (stability) on these timescales, peak-to-peak potential separations (i.e. ΔE_p), however, exceed 59/*n* mV (where *n* is the number of electrons transferred). Further, both ΔE_p and $E_p{}^c$-$E_{p/2}{}^c$ (where $E_{p/2}{}^c$ represents the cathodic potential at half peak height) are found to increase consistently with increasing scan rates. This feature is commonplace within *neat* IL electrolytes wherein the process kinetics and mass transport may be mutually sluggish and the overall O_2 reduction process is *quasi*-reversible.[61–63] Plots of the cathodic reduction peak current density, $j_p{}^c$ vs. $v^{1/2}$ revealed mostly linear dependencies on the current magnitude with significant deviations occurring only at the higher scan rates. Plots $j_p{}^c$ vs. $v^{1/2}$ for each studied electrolyte are shown in Figure S7 in the ESI along with the respective CV traces. Within each of these plots, the experimental current density peaks are compared with theoretical values based on the Randles-Ševćik equations for reversible systems

$$j^c_{p,rev} = -0.446nFC(nFDv/RT)^{0.5} \quad [16]$$

where $n = 1$ or 2 and for quasi-reversible systems

$$j^c_{p,quasi} = -0.496nFC(\alpha nFDv/RT)^{0.5} \quad [17]$$

where *j* represents the current density in A · cm^{-2}, *F* is the Faraday constant, *C* and *D* represent the analyte concentration (in units of mol · cm^{-3}) and diffusion coefficient (in units of $cm^2 \cdot s^{-1}$), respectively, α represents an approximation of the transfer coefficient, *v* represents the scan rate (in units of V · s^{-1}) and *R* and *T* represent the molar gas constant (8.3145 J · mol · K^{-1}) and the absolute temperature, respectively. The value utilized for α was estimated, from the shape of the O_2 reduction curve, using the equation[64,65]

$$E^c_p - E^c_{p/2} = 1.857RT/\alpha nF \quad [18]$$

where all symbols are as defined previously and $E_p{}^c$-$E_{p/2}{}^c$ is given in volts. These plots show that, particularly for the for the cathodic peaks, a general linear dependence in agreement with Equations 16 and 17 where $n = 1$, indicative of a single electron transfer process, as expected. However, deviations below $j_p{}^c{}_{rev}$ are consistently observed at higher scan rates.

For the two neat IL electrolytes, where the $O_2/O_2{}^{\bullet-}$ couple appears chemically reversible, treatment of the derived CV data by the Nicholson method affords an approximation of the heterogeneous electron transfer rate constant, k_o, by application of the relationship

$$\psi = k_o[\pi nDFv/RT]^{-0.5} \quad [19]$$

where the symbols within the brackets are as defined previously and ψ represents the kinetic parameter dependent on the peak potential separations, ΔE_p.[66] Values for ψ, applicable where $\Delta E_p <$ ca. 250 mV, were estimated using Equation 20 proposed by Lavagnini et al.[67] as a correlation of the original working curves constructed by Nicholson.[66]

$$\psi = \frac{(-0.6288 + 0.0021\Delta E_p)}{(1 - 0.017\Delta E_p)} \quad [20]$$

The slope of the ψ vs. $[\pi nDFv/RT]^{-0.5}$ plots, shown in Figure S8 in the ESI, provides an approximation of 0.7 × 10^{-3} cm · s^{-1} and 1.2 × 10^{-3} cm · s^{-1} for the k_o value of O_2 reduction in [$Pyrr_{14}$][TFSI] and [N_{1124}][TFSI], respectively. However, a pre-requisite of this methodology is complete compensation for any *iR*-drop within the experiment which, qualitatively, appears insufficient for the [$Pyrr_{14}$][TFSI] IL and, thus, would yield an under-estimation for k_o. In support of this, by simulation of the CV traces at 50 mV · s^{-1} using the EC-Lab software, and a simple E-mechanism only, good agreement between simulation and experiment is only achieved when an additional ca. 500 Ω is introduced (Figure S9 in the ESI). Post-processing of E_p values for [$Pyrr_{14}$][TFSI] using $E_p(corr) = E_p + i_pR$ and R = 500 Ω followed by Nicholson treatment using the corrected $E_p(corr)$ values affords a crude approximation of k_o = 1.1 × 10^{-3} cm · s^{-1}.

Peak information relating to the 20 mV · s^{-1} CV traces shown in Figure 7a and 7b is provided in Table II as a function of the mole fraction of IL. As the proportion of TEGDME is increased, the reductive charge passed decreases initially but increases significantly

Table II. Peak information for the 20 mV · s^{-1} scan rate CVs of O_2-saturated (*X*)IL – (1-*X*)TEGDME binary mixtures; E_p,j_p and *Q* represent the peak potentials, peak currents and peak integral charge where the superscript *c* and *a* represent the cathodic and anodic processes, respectively; ΔE_p and $E_{1/2}$ represent the peak-to-peak potential separation ($E_p{}^a - E_p{}^c$) and an estimation of the formal redox potential ($[E_p{}^c + E_p{}^a]/2$), respectively; and $j_p{}^a / j_p{}^c$ and Q^a/Q^c represent the ratio between the cathodic and anodic peak current densities and charge passed, respectively.

X_{IL}	$E_p{}^c$ / V vs. Fc^+/Fc	$E_p{}^a$ / V vs. Fc^+/Fc	ΔE_p / V	$E_{1/2}$ / V vs. Fc^+/Fc	$j_p{}^c$ / mA · cm^{-2}	$j_p{}^a / j_p{}^c$	Q^a/Q^c
			[$Pyrr_{14}$][TFSI]				
1	−1.31	−1.14	0.17	−1.22	−0.65	1.00	0.99
0.9	−1.28	−1.16	0.12	−1.22	−0.51	0.86	0.70
0.8	−1.28	−1.17	0.10	−1.22	−0.61	0.75	0.49
0.6	−1.27	−1.17	0.10	−1.22	−0.76	0.50	0.33
0.4	−1.29	−1.16	0.13	−1.22	−0.83	0.25	0.14
			[N_{1124}][TFSI]				
1	−1.26	−1.14	0.13	−1.20	−0.56	1.01	1.00
0.4	−1.26	−1.14	0.12	−1.20	−1.08	0.38	0.25

for the higher TEGDME fractions (where $X_{IL} = 0.6$ and 0.4). This trend is simply attributed to a trade-off between O_2 solubility, which is highest at low TEGDME fractions, and O_2 diffusivity which compensates the O_2 supply capability at higher TEGDME fractions. Further, as shown in Table II, ΔE_p tends to decrease with the addition of TEGDME solvent. However, more critically is the uniform reduction in the oxidative peak magnitude on the return sweep. As highlighted by the ratios between the peak current densities ($j_p{}^a$ / $j_p{}^c$) and the oxidative and reductive charges (Q^a/Q^c), which decrease almost linearly as a function of the TEGDME mole fraction, the presence of the glyme solvent appears to drastically affect the chemical stability of the $O_2/O_2^{\bullet\cdot}$ couple in these mixtures. This is indicative of a coupled irreversible homogeneous chemical reaction following the electroreduction between the reduced species and the TEGDME solvent. Additionally, peak current ratios $i_p{}^a{}_0/i_p{}^c{}_0$ (where i_{p0} represents the peak currents as estimated from a $y(i) = 0$ Ampere baseline) in the high TEGDME fraction blends were found to increase at increasing scan rates. Using Nicholson's semi-empirical relationship between experimentally observed peak currents and the rate of a coupled homogeneous process,[68] the apparent rate constant derived for the 20 $mV \cdot s^{-1}$ scans appears to increase exponentially with the concentration of the TEGDME component (shown in Figure S10 in the ESI). However, the non-Cottrellian decay of the negative current following the cathodic peak makes estimation of the current at the switching potential difficult to define.

Within ILs, like $[Pyrr_{14}][TFSI]$, the superoxide is considered to be effectively stabilized through reversible Coulombic interactions with the IL cationic center.[69] Anodic potential shifts of $E_{1/2}$ for the neat $[N_{1124}][TFSI]$ relative to $[Pyrr_{14}][TFSI]$ IL are indicative stronger or more effective $O_2^{\bullet-}$-coordination (by the IL cation), though the magnitude of the shift (20 mV) is minimal. However, the anodic shift for the onset potential of O_2 reduction as the quantity of TEGDME is increased may further support the presence of unwanted irreversible decomposition reactions between solvent and reduced species. Such anodic shifts, coupled with loss of chemical reversibility of the $O_2/O_2^{\bullet-}$, have been observed in IL systems which have been doped with water,[70] or other protic additives, e.g. HCl,[63] ethylene glycol.[71] Therein, as observed also in protic ILs,[72,73] the superoxide radical acts as a reasonably strong base and undergoes reactions with the labile protons leading to the formation of hydroperoxyl anions and hydrogen peroxide. In certain systems this chemistry is partially reversible, creating implications for energy storage systems based on O_2/H_2O_2 conversion reactions.[74] However, any such proton abstraction or ether hydroperoxide formation in the TEGDME blends observed here is likely coupled with complex decomposition pathways, as reported previously,[75] and would be limiting for any stable longer-term usage of these materials in sensor applications, for example.

Conclusions

In this work, we have described a series of investigations into the thermophysical and electrochemical properties of IL/molecular solvent binary mixtures, with the general formula (*X*)IL – (1-*X*) TEGDME, as potential electrolyte formulations for electrochemical energy storage devices and amperometric O_2 sensors. The mixtures are based on a TEGDME molecular solvent component blended with one of two cyclic and acyclic alkylammonium bis{(trifluoromethyl)sulfonyl}imide-based ILs, $[Pyrr_{14}][TFSI]$ and $[N_{1124}][TFSI]$, respectively. The two neat ILs, differing in molecular mass by only a single carbon atom on the cation, exhibit very similar bulk viscosities and electrochemical stabilities but the acyclic analogue, $[N_{1124}][TFSI]$, exhibits slightly poorer conductivity. Thermophysical characterization of a wide range of binary mixture formulations and temperatures firstly highlights the important potential for enhancement of the sluggish transport properties typically exhibited by neat ILs. Secondly, comparison of the two ILs within equivalent mole fraction ($x_{IL} = 0.4$) binary mixtures reveals similar enhancements in the measured properties. Assessment of the Walden-type behavior of the mixtures shows that the effective reductions in IL viscosities upon addition of the TEGDME solvent appears insufficiently balanced by the enhancements in electrolytic conductivity, potentially indicative of the solvation of ion pairs rather than promoting dissociation of the counterions.

Measurements of the O_2 supply capabilities of the binary mixture formulations firstly reveal that even small quantities of the TEGDME solvent can affect significant reductions in the moderate solubility of the gas within the IL. However, as expected, addition of the molecular solvent affords more significant promotions in the diffusivity of the dissolved O_2. Macro-electrode (GC) voltammetry of the oxygen reduction show mass transport and electron transfer kinetics of oxygen reduction are mutually sluggish within the *neat* ILs. However, these experiments revealed more significant issues relating to the chemical reversibility of the oxygen/superoxide couple in the blended electrolytes, suggesting decomposition reactions with the TEGDME solvent consume the superoxide radical even in the short timescale of the reported cyclic voltammetry experiments. Ultimately, while the TEGDME solvent favorably, though somewhat modestly, promotes important transport properties of the ILs, the results further highlight the importance of the pursuit for new, highly stable, electrolyte solvent materials.

Acknowledgments

The authors would like to gratefully acknowledge the funding from EPSRC (EP/L505262/1) and Innovate UK for the Practical Lithium-Air Batteries project (project number: 101577).

References

1. A. Balducci, S. S. Jeong, G. T. Kim, S. Passerini, M. Winter, M. Schmuck, G. B. Appetecchi, R. Marcilla, D. Mecerreyes, V. Barsukov, V. Khomenko, I. Cantero, I. De Meatza, M. Holzapfel, and N. Tran, *J. Power Sources*, **196**(22), 9719 (2011).
2. R. S. Kühnel, N. Böckenfeld, S. Passerini, M. Winter, and A. Balducci, *Electrochim. Acta*, **56**(11), 4092 (2011).
3. L. Lombardo, S. Brutti, M. A. Navarra, S. Panero, and P. Reale, *J. Power Sources*, **227**, 8 (2013).
4. B. Yang, C. Li, J. Zhou, J. Liu, and Q. Zhang, *Electrochim. Acta*, **148**, 39 (2014).
5. C. Arbizzani, M. Biso, D. Cericola, M. Lazzari, F. Soavi, and M. Mastragostino, *J. Power Sources*, **185**(2), 1575 (2008).
6. T. Abdallah, D. Lemordant, and B. Claude-Montigny, *J. Power Sources*, **201**, 353 (2012).
7. A. Krause and A. Balducci, *Electrochem. Commun.*, **13**(8), 814 (2011).
8. S. Pohlmann, T. Olyschläger, P. Goodrich, J. A. Vicente, J. Jacquemin, and A. Balducci, *Electrochim. Acta*, **153**, 426 (2015).
9. C. Schütter, A. R. Neale, P. Wilde, P. Goodrich, C. Hardacre, S. Passerini, J. Jacquemin, and A. Balducci, *Electrochim. Acta*, **220**, 146 (2016).
10. V. Ruiz, T. Huynh, S. R. Sivakkumar, and A. G. Pandolfo, *RSC Adv.*, **2**(13), 5591 (2012).
11. C. Wolff, S. Jeong, E. Paillard, A. Balducci, and S. Passerini, *J. Power Sources*, **293**, 65 (2015).
12. C. Ding, T. Nohira, R. Hagiwara, K. Matsumoto, Y. Okamoto, A. Fukunaga, S. Sakai, K. Nitta, and S. Inazawa, *J. Power Sources*, **269**, 124 (2014).
13. D. Monti, A. Ponrouch, M. R. Palacín, and P. Johansson, *J. Power Sources*, **324**, 712 (2016).
14. H. Nakamoto, Y. Suzuki, T. Shiotsuki, F. Mizuno, S. Higashi, K. Takechi, T. Asaoka, H. Nishikoori, and H. Iba, *J. Power Sources*, **243**, 19 (2013).
15. G. A. Elia, J. Hassoun, W. J. Kwak, Y. K. Sun, B. Scrosati, F. Mueller, D. Bresser, S. Passerini, P. Oberhumer, N. Tsiouvaras, and J. Reiter, *Nano Lett.*, **14**(11), 6572 (2014).
16. M. C. Buzzeo, C. Hardacre, and R. G. Compton, *Anal. Chem.*, **76**(15), 4583 (2004).
17. Z. Wang, P. Lin, G. A. Baker, J. Stetter, and X. Zeng, *Anal. Chem.*, **83**(18), 7066 (2011).
18. P. Li and R. G. Compton, *Electroanalysis*, **27**(7), 1550 (2015).
19. R. Toniolo, N. Dossi, A. Pizzariello, A. P. Doherty, S. Susmel, and G. Bontempelli, *J. Electroanal. Chem.*, **670**, 23 (2012).
20. M. C. Buzzeo, O. V. Klymenko, J. D. Wadhawan, C. Hardacre, K. R. Seddon, and R. G. Compton, *J. Phys. Chem. B*, **108**(12), 3947 (2004).
21. B. A. Rosen, A. Salehi-Khojin, and R. I. Masel, *in* "*2010 IEEE Sensors*,", p. 365, 2010.
22. P. Kuberský, J. Altšmíd, A. Hamáček, S. Nešpůrek, and O. Zmeškal, *Sensors*, **15**(11), 28421 (2015).
23. J. Ding, D. Zhou, G. Spinks, G. Wallace, S. Forsyth, M. Forsyth, and D. MacFarlane, *Chem. Mater.*, **15**(12), 2392 (2003).
24. B. J. Akle, M. D. Bennett, and D. J. Leo, *Sensors and Actuators A: Physical*, **126**(1), 173 (2006).
25. S. Imaizumi, H. Kokubo, and M. Watanabe, *Macromolecules*, **45**(1), 401 (2012).

26. A. P. Abbott and K. J. McKenzie, *Phys. Chem. Chem. Phys.*, **8**(37), 4265 (2006).
27. S. Zein El Abedin and F. Endres, *ChemPhysChem*, **7**(1), 58 (2006).
28. R. Al-Salman, S. Z. El Abedin, and F. Endres, *Phys. Chem. Chem. Phys.*, **10**(31), 4650 (2008).
29. E. Coadou, P. Goodrich, A. R. Neale, L. Timperman, C. Hardacre, J. Jacquemin, and M. Anouti, *ChemPhysChem*, **17**(23), 3992 (2016).
30. Z. -B. Zhou, H. Matsumoto, and K. Tatsumi, *Chem-Eur. J.*, **12**(8), 2196 (2006).
31. K. Tsunashima and M. Sugiya, *Electrochem. Commun.*, **9**(9), 2353 (2007).
32. A. Khan and C. Zhao, *Electrochem. Commun.*, **49**(0), 1 (2014).
33. S. Ferrari, E. Quartarone, C. Tomasi, M. Bini, P. Galinetto, M. Fagnoni, and P. Mustarelli, *J. Electrochem. Soc.*, **162**(2), A3001 (2015).
34. J. Xie, Q. Dong, I. Madden, X. Yao, Q. Cheng, P. Dornath, W. Fan, and D. Wang, *Nano Lett.*, **15**(12), 8371 (2015).
35. N. Ab Manan, C. Hardacre, J. Jacquemin, D. W. Rooney, and T. G. A. Youngs, *J. Chem. Eng. Data*, **54**(7), 2005 (2009).
36. A. R. Neale, P. Li, J. Jacquemin, P. Goodrich, S. C. Ball, R. G. Compton, and C. Hardacre, *Phys. Chem. Chem. Phys.*, **18**(16), 11251 (2016).
37. M. S. Shannon, J. M. Tedstone, S. P. O. Danielsen, M. S. Hindman, A. C. Irvin, and J. E. Bara, *Ind. Eng. Chem. Res.*, **51**(15), 5565 (2012).
38. M. Sharp, *Electrochim. Acta*, **28**(3), 301 (1983).
39. Y. Wang, E. I. Rogers, and R. G. Compton, *J. Electroanal. Chem.*, **648**(1), 15 (2010).
40. D. Shoup and A. Szabo, *J. Electroanal. Chem. Interfacial Electrochem.*, **140**(2), 237 (1982).
41. F. M. Gaciño, T. Regueira, L. Lugo, M. J. P. Comuñas, and J. Fernández, *J. Chem. Eng. Data*, **56**(12), 4984 (2011).
42. K. R. Harris, L. A. Woolf, M. Kanakubo, and T. Rüther, *J. Chem. Eng. Data*, **56**(12), 4672 (2011).
43. A. Pal and H. Kumar, *J. Mol. Liq.*, **89**(1), 189 (2000).
44. S. K. Chaudhari, K. R. Patil, J. Allepús, and A. Coronas, *Fluid Phase Equilib.*, **108**(1), 159 (1995).
45. W. Xu, E. I. Cooper, and C. A. Angell, *J. Phys. Chem. B*, **107**(25), 6170 (2003).
46. K. Ueno, H. Tokuda, and M. Watanabe, *Phys. Chem. Chem. Phys.*, **12**(8), 1649 (2010).
47. C. Schreiner, S. Zugmann, R. Hartl, and H. J. Gores, *J. Chem. Eng. Data*, **55**(5), 1784 (2010).
48. A. Hofmann, M. Migeot, L. Arens, and T. Hanemann, *Int. J. Mol. Sci.*, **17**(5), 670 (2016).
49. P. M. Bayley, G. H. Lane, N. M. Rocher, B. R. Clare, A. S. Best, D. R. MacFarlane, and M. Forsyth, *Phys. Chem. Chem. Phys.*, **11**(33), 7202 (2009).
50. W. Li, Z. Zhang, B. Han, S. Hu, Y. Xie, and G. Yang, *J. Phys. Chem. B*, **111**(23), 6452 (2007).
51. M. C. Buzzeo, R. G. Evans, and R. G. Compton, *ChemPhysChem*, **5**(8), 1106 (2004).
52. F. Béguin, V. Presser, A. Balducci, and E. Frackowiak, *Adv. Mater. (Weinheim, Ger.)*, **26**(14), 2219 (2014).
53. H. G. Jung, J. Hassoun, J. B. Park, Y. K. Sun, and B. Scrosati, *Nat. Chem.*, **4**(7), 579 (2012).
54. X. -J. Huang, E. I. Rogers, C. Hardacre, and R. G. Compton, *J. Phys. Chem. B*, **113**, 8953 (2009).
55. J. Read, K. Mutolo, M. Ervin, W. Behl, J. Wolfenstine, A. Driedger, and D. Foster, *J. Electrochem. Soc.*, **150**(10), A1351 (2003).
56. C. Hardacre, C. Mullan, and T. G. A. Youngs, in *Ionic Liquids Completely UnCOILed: Critical Expert Overviews*, N. V. Plechkova and K. R. Seddon, eds., p. 55., Wiley & Sons, Inc., New Jersey, USA, (2016).
57. R. Hayes, G. G. Warr, and R. Atkin, *Chem. Rev. (Washington, DC, U. S.)*, **115**(13), 6357 (2015).
58. F. Castiglione, A. Famulari, G. Raos, S. V. Meille, A. Mele, G. B. Appetecchi, and S. Passerini, *J. Phys. Chem. B*, **118**(47), 13679 (2014).
59. K. Hayamizu, E. Akiba, T. Bando, and Y. Aihara, *J. Chem. Phys.*, **117**(12), 5929 (2002).
60. F. Castiglione, M. Moreno, G. Raos, A. Famulari, A. Mele, G. B. Appetecchi, and S. Passerini, *J. Phys. Chem. B*, **113**(31), 10750 (2009).
61. S. Monaco, A. M. Arangio, F. Soavi, M. Mastragostino, E. Paillard, and S. Passerini, *Electrochim. Acta*, **83**, 94 (2012).
62. Y. Katayama, K. Sekiguchi, M. Yamagata, and T. Miura, *J. Electrochem. Soc.*, **152**(8), E247 (2005).
63. C. Pozo-Gonzalo, P. C. Howlett, J. L. Hodgson, L. A. Madsen, D. R. MacFarlane, and M. Forsyth, *Phys. Chem. Chem. Phys.*, **16**(45), 25062 (2014).
64. R. S. Nicholson and I. Shain, *Anal. Chem.*, **36**(4), 706 (1964).
65. R. J. Klingler and J. K. Kochi, *J. Phys. Chem.*, **85**(12), 1731 (1981).
66. R. S. Nicholson, *Anal. Chem.*, **37**(11), 1351 (1965).
67. I. Lavagnini, R. Antiochia, and F. Magno, *Electroanalysis*, **16**(6), 505 (2004).
68. R. S. Nicholson, *Anal. Chem.*, **38**(10), 1406 (1966).
69. C. J. Allen, J. Hwang, R. Kautz, S. Mukerjee, E. J. Plichta, M. A. Hendrickson, and K. M. Abraham, *J. Phys. Chem. C*, **116**(39), 20755 (2012).
70. C. Pozo-Gonzalo, A. A. J. Torriero, M. Forsyth, D. R. MacFarlane, and P. C. Howlett, *J. Phys. Chem. Lett.*, **4**(11), 1834 (2013).
71. C. Pozo-Gonzalo, C. Virgilio, Y. Yan, P. C. Howlett, N. Byrne, D. R. MacFarlane, and M. Forsyth, *Electrochem. Commun.*, **38**, 24 (2014).
72. D. A. Walsh, A. Ejigu, J. Smith, and P. Licence, *Phys. Chem. Chem. Phys.*, **15**(20), 7548 (2013).
73. A. Khan, X. Lu, L. Aldous, and C. Zhao, *J. Phys. Chem. C*, **117**(36), 18334 (2013).
74. C. Pozo-Gonzalo, M. Kar, E. Jónsson, P. C. Howlett, D. R. MacFarlane, and M. Forsyth, *Electrochim. Acta*, **196**, 727 (2016).
75. V. S. Bryantsev and F. Faglioni, *J. Phys. Chem. A*, **116**(26), 7128 (2012).